Figure Captions

Chapter 1

Fig 1.1 Transmission distance in silica fiber versus transmission speed for different wavelengths of available lasers

Fig 1.2 The lattice parameters and band gap energies of the selected III-V binary and their alloys.

Fig 1.3 The schematic of a Fabry –Perot cavity laser.

Fig 1.4 A VCSEL structure with the DBR mirrors with active region, and light travels perpendicular through the thin active region

Chapter 2

Fig 2.1 The schematic of the process chamber and it`s components.

Fig 2.2 Schematic of sources shutters and substrate position in the MBE chamber.

Fig 2.3 Schematic digrams of the growth modes for semiconductor system (a) Frank-van der merwe (FM, layaer by layer);(b) Stranski-Krastanow (SK, island with the wetting layer);(c) Volmer-Weber (VW, island)

Fig 2.4 The RT-PL spectrum of all samples with different indium growth rate.

Fig 2.5 RT-PL spectra of InAs/InGaAs/GaAs QDs under difference As beam flux

Fig 2.6 The AFM images of InAs/InGaAs/GaAs Dot in Well structure. ($6x10^{10}/cm^2$)

Fig 2.7 RT-PL spectra of InAs Dot in well structure varied indium composition in the quantum well.

Fig 2.8 RT-PL spectra of InAs/GaAs QDs and with covered InGaAsQW.

Fig 2.9 The schematic depicts the structure of the samples in band diagram from A to D

Fig 2.10 The RT-PL spectra of the samples (A to D) with InAs/InAlAs/InGaAs/GaAs QDs active region.

Fig 2.11 1.0 x 1.0 μm^2 atomic force microscopic image of a sample with 2.6 ML InAs

QDs covered with 10 Å InAlAs/44 Å InGaAs strain reduce layer.

Fig 2.12 RT-PL spectra of InAs/InAlAs/InGaAs/GaAs structure under 15 and 90mW excited power.

Fig 2.13 Energy separations of InAs QDs covered with InAlAs strain reduce layer between ground state and first excited state.

Fig 2.14 The line-width of ground state and excited state of InAs / InAlAs / InGaAs / GaAs active region.

Chapter 3

Fig 3.1 RT-PL spectra for samples with one QD layer formed by depositing different amount of single InAs (2.8 ML) QDs and InAs (2.6~2.8ML), covered with 5-nm-thick $In_{0.15}Ga_{0.85}As$ layer. Excited state (ES) and ground state (GS) peak position shifts toward longer wavelength when the thickness of InAs is increasing.

Fig 3.2 SEM image of 5 pairs InAs/InGaAs/GaAs QDs layers with the 30nm GaAs spacer layer.

Fig 3.3 Dependence of the threshold current density on the cavity length for 10-μm-width stripe lasers with as-cleaved facets. The emitting wavelength at 1.22 μm with the excited lasing.

Fig 3.4 The L-I-V curve of QDs edge emitting lasers in 5μm ridge with 3mm cavity length under pulsed operation at room temperature.

Fig. 3.5 Dependences of total output power (P_{out}) and voltage (V) for a 3-mm-long and 5-μm-wide ridge waveguide diode, with as-cleaved facets. Lasing spectrum above the threshold and far-field pattern in vertical direction are shown in the inserts.

Fig 3.6 The temperature characteristics of QDs lasers in 10μm ridge wide and 5mm cavity length.

Fig 3.7 Schematic diagram of QD laser structure with narrow ridge waveguide, and

cross-sectional TEM image of ECVQD active region.

Fig 3.8 The L-I curve of a 10-pair vertical coupled InAs/GaAs QDs laser with a 17nm GaAs space layer. The laser dimensions are 50μm wide ridge and 2mm in length. The insert shows the lasing spectrum.

Fig 3.9 Dependence of threshold current density of the lasers on the cavity length, with a 50μm ridge width.

Fig 3.10 The dependence of the reciprocal external differential quantum efficiency on the cavity length for the 50 μm-wide devices under pulsed operation at room temperature.

Fig. 3.11 (a) EL spectra of a 3 μm-wide, 500 μm-long device at different injection current densities under pulsed operation.

Fig. 3.11 (b) Lasing spectra of 3 μm-wide, 2 mm-long cavity devices at an injection current of 1 A under CW operation. The dashed line shows a lasing spectrum for a similar ten stacks 1.3 μm QD laser with a conventional uncoupled InAs/InGaAs/GaAs QD active region.

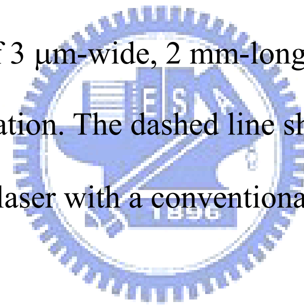

Fig 3.12 (a) The structure design of three groups of 3-layer QDs in the active region.

Fig 3.12 (b) InAs/InGaAs/GaAs QDs are periodically positioned in the anti-node of the optical field.

Fig 3.13 The schematic of fully doped VCSELs with InAs/InGaAs/GaAs QDs active media.

Fig 3.14 (a) Room temperature CW single mode lasing at threshold current below 1 mA with 5.5 μm aperture size.

Fig 3.14 (b) Single mode CW lasing spectrum of QDs VCSELs under different driving current.

Chapter 4

Fig 4.1 The schematic of the N-plasma system and N_2 gas injection system.

Fig 4.2 The front views of plasma source with mounted PBN plate.

Fig 4.3 Bandgap versus lattice constant graph for III–V alloys showing lines of lattice match to GaAs for nitride–arsenide alloys and to InP for arsenide–phosphide alloys in the region applicable to long-wavelength fiber systems.

Fig 4.4 The Photoluminescence (PL) setup designed for the optical properties measurements.

Fig 4.5 Dependence of N composition of GaAsN layers on plasma condition **(a)** plasma light intensity at different GaAs growth rates and different aperture layouts. Growth rates are shown as numbers on corresponding curve.

Fig 4.5 (b) N content vs parameter C_{SOURCE}

Fig 4.6 Dependence of RT-PL position on nitrogen content, with 0.2 μm-thick GaAsN layers. Insert shows the substrate temperature dependence on the emission wavelength red shift.

Fig 4.7 (a) The RT-PL emission wavelength and PL intensity of GaAsN bulk material dependence on the nitrogen composition.

Fig 4.7 (b) Plot of XRD spectra and the corresponding PL emission wavelength of the GaAsN bulk material with nitrogen content of 0.5%,0.9%,1.4% and 5.6%.

Fig 4.8 PL peak intensity and peak FWHM versus substrate temperature of the grown GaAsN layer. A window between the growth substrate temperatures with optical quality affects the material quality.

Fig 4.9 Photograph of wafers with GaAsN bulk material deposited on GaAs substrate. The wafer on the right side was grown with too high substrate temperature, the wafer on the left side was grown in the correct region temperature.

Fig 4.10 (a) RHEED images of GaAsN thin film, grown with too high and suitable temperature.

Fig 4.10 (b) Dependence of Growth rate and PL intensity. Plasma condition was kept constant for all samples.

Fig 4.11 Dependence of integrated PL intensity of the GaAsN and GaAs layers on the growth temperature.

Fig 4.12 (a) Schematic diagram of DLTS and CV electrical measurement.

Fig 4.12 (b) Schematic of MBE growth structure for optical measurements.

Fig 4.13 (a) Dependence of PL intensity on the annealing temperature

Fig 4.13 (b) The emission wavelength dependence on the annealing temperature

Fig 4.14 The DLTS spectra of as-grown InGaAsN/GaAs quantum well.

Fig 4.15 The TEM images of InGaAsN/GaAs quantum well with as grown and at 750^0C after 30 mins thermal treatment. Dark-field TEM-images before **(a)** and after thermal annealing **(b)**, which show contrast-fluctuations of a length-scale.

Fig 4.16 TEM images of InGaAsN/GaAs quantum well grown at substrate temperature of 450^0C and 420^0C.

Fig 4.17 RT-PL spectra of InGaAsN/GaAs QWs grown at high and low growth rates.

Fig 4.18 DLTS spectra present the impurities level of as grown sample of InGaAsN/GaAs QWs and after 750^0C 10mins thermal annealing.

Fig 4.19 The RT-PL spectra of GaAsN/InGaAsN/GaAsN QWs with GaAsN strain-compensation layer.

Fig 4.20 The schematic structure of PL measured sample with InGaAsN(sb)/GaAs QW

Fig 4.21 The HRXRD spectra of InGaAs/GaAs, InGaAs(Sb)/GaAs, InGaAsN/ GaAs and InGaAsN(Sb)/GaAs highly strained MQWs.

Fig 4.22 The PL spectra of the as grown samples with InGaAs/GaAs and InGaAsSb QWs active region.

Fig 4.23 RT-PL spectra of as grown and InGaAs/GaAs MQWs of RTA treatment at

800^0C 3 mins.

Fig 4.24 The RT-PL spectra of 3 pairs InGaAs/GaAs quantum wells by adding the Sb material into.

Fig 4.25 The RT-PL spectra of InGaAsN/GaAs and InGaAsNSb/GaAs MQWs with different Sb doping level after RTA annealing.

Chapter 5

Fig 5.1 The schematic diagram of L-I measurement system.

Fig 5.2 The image of laser measurement system.

Fig 5.3 The L-I-V curve of 50μm-ridge broad area lasers. The insert shows the lasing spectra.

Fig 5.4 Dependence of threshold current density and reverse cavity length of InGaAsN/GaAs broad are edge emitting lasers.

Fig 5.5 The threshold current density versus the reciprocal cavity length for 1.3μm InGaAsN ridge waveguide lasers with 3μm width under pulsed operation at room temperature.

Fig 5.6 An internal quantum efficiency with an internal loss exacted from a 50μm with 1 mm cavity length laser.

Fig 5.7 Cross sectional SEM image of the InGaAsN/GaAs laser structure.

Fig 5.8 Dependence of total output power recorded on threshold current in pulsed regime for RW stripe. *I-V* curve and conversion efficiency are also shown.

Fig 5.9 L-I-V characteristics of the InGaAsN laser under CW operation of RW diode after facet coating, bonding, and packaging in TO46 can.

Fig 5.10 (a) Far field patterns of the InGaAsN under single mode operation up to the highest power recorded.

Fig 5.10 (b) Measured lasing spectra of the InGaAsN laser, the lasing spectra are

getting wider with drive current and shifts to 1.31 μm at high power.

Fig 5.11 (a) The schematic of intra cavity contacted InGaAsN/GaAS VCSELs.

Fig 5.11 (b) The spectra of measured and simulated reflectance of the VCSELs sample.

Fig 5.12 (a) The reflection spectra of VCSELs that included the normalized PL spectrum of InGaAsN/GaAs QWs active region.

Fig 5.12 (b) Cross-sectional SEM photographs show the two steps etched sidewall of 1.3μm InGaAsN Intra cavity contacted VCSEL grown by MBE.

Fig 5.13 The L-I-V curve of the intra cavity VCSEL with 18 μm oxided aperture size.

Fig 5.14 The RT-CW L-I-V curves of the single mode intra-cavity contacted InGaAsN/GaAs QW VCSELs with a current aperture of 7 μm.

Fig 5.15 The threshold current under CW operation and lasing wavelength under pulsed operation as a function of the operation temperature.